Hindawi
Advances in Civil Engineering
Volume 2022, Article ID 8471016, 21 pages
https://doi.org/10.1155/2022/8471016

Research Article

Mechanical Behavior of Q460 High-Strength Steel under Low-Cycle Fatigue Loading

Xue Han,[1] Min Chang,[2] Haifeng Li ,[2,3] Hualin Cao,[2] and Baoan Cao[2]

[1]*Xiamen Institute of Technology, Xiamen 361021, China*
[2]*College of Civil Engineering, Huaqiao University, Xiamen 361021, China*
[3]*Key Laboratory for Intelligent Infrastructure and Monitoring of Fujian Province (Huaqiao University), Jimei Avenue 668, Xiamen, Fujian 361021, China*

Correspondence should be addressed to Haifeng Li; lihai_feng@126.com

Received 2 December 2021; Accepted 4 July 2022; Published 18 August 2022

Academic Editor: Nicola Baldo

To investigate the mechanical properties of Q460 high-strength steel under repeat tensile loading, 45 specimens were prepared for repeated tensile tests. The specimens are tested under 16 different loading regimes. The effects of welded joints, specimen shape and dimensions, and loading modes on the mechanical properties of the steel were analyzed. In addition, a finite element model of the specimen under cyclic load was established with ANSYS and the numerical results were compared with those of the experimental tests. This finite element model can accurately simulate the deformation characteristics of Q460 steel specimens. Experimental studies have found that the welded joints have adverse effects on the mechanical properties of this material. The cumulative effect of fatigue damage on the welded specimens was significant, and the ductility of welded specimens was poor under cyclic loading. The loading mode had a major impact on the results of the material tests. As the number of loading cycles increased, the cumulative effect of fatigue damage on the specimens was more evident, and the length, size, and cross-sectional shape of the tensile zone all affected the stiffness of the specimen. Finally, based on the experimental research and numerical analysis results, a design formula for the tensile strength of Q460 steel under repeated loading was proposed. This formula can serve as a reference for the application of Q460 steel in seismic engineering.

1. Introduction

High-strength steel generally refers to steel with a yield strength of 460 MPa or greater. Applying high-strength steel in structures can reduce the size of the components and the quantity of steel required, thereby decreasing the structural weight and seismic hazard. Some work has been carried out to prove quality control and strength of steel have a major impact on the seismic performance of steel space structures (Dai et al. [1]). Using high-strength steel as building material can also satisfy the new requirements of energy-saving, emission reduction, and the low-carbon environment. With the significant progress in the energy-absorbing and damping technology, high-strength and ultrahigh-strength steels are widely used in the design of steel structures (Bjorhovde [2]). Nowadays, high-strength steel has been used as the main structural material in large-scale construction projects, such as the Sony Center Building in Berlin, Latitude Building in Sydney, Australia, and Landmark Tower in Japan. Therefore, the safety problem of large steel structure building is particularly important, and some scholars studied the collapse of steel high-rise buildings caused by large earthquakes and its anticollapse mechanism (Lin et al. [3]). Meanwhile, the failure mechanism of high-strength structural steels under high-stress low-cycle fatigue loads has received attention from scholars of various research fields.

Researchers worldwide have performed many studies on the constitutive models and mechanical properties of high-strength steels. Some scholars have studied the mechanical properties of high-strength steel materials and the constitutive models of tested steel under monotonic or cyclic

loading [4–6]. Nie et al. [7] studied the mechanical properties of steel on cold-formed steel (CFS) structures at high temperature and proposed constitutive relationship models based on the test data of S350, S420, and G500 steel, respectively. Hu et al. [8] analyzed the average elastic modulus of H-beam members according to the influence of damage on the elastic modulus of steel obtained from the mechanical test of damaged steel. The formulas for calculating the average elastic modulus of damaged H-beams under different damage degrees were calculated. Wang et al. [9] compared the constitutive relationship among low yield point steel, ordinary-strength steel (Q345B), and high-strength steel (Q460D). Li et al. [10] studied the ductile failure mode of Q460 high-strength structural steel under quasi-static conditions. Their results indicated that the fracture mechanism of this steel varied in different stress triaxial regions. Scholars mostly analyze the properties of steel components by studying the constitutive models of steel components.

Some scholars have conducted experimental investigations on the mechanical properties of welded test specimens of high-strength steels under monotonic and cyclic loading. Haslberger et al. [11] conducted a study on the microstructure and mechanical properties of high-strength steel welding consumables with a minimum yield strength of 1100 MPa; a concept for toughening and strengthening all-weld metal samples was presented. Ozturk Yilmaz et al. [12] studied the effect of welding parameters on the microstructure and mechanical properties of different resistance spot-welded DP1000-QP1180 simulation joints. The results indicated that the spot-welded joints with higher strengths exhibited a more ductile fracture characteristic. Sowards et al. [13] performed an experimental study regarding the mechanical properties of low-alloy high-strength steel sheets. The results revealed that the low-cycle fatigue strength of the weld was considerably higher than that of the base metal. Peilei et al. [14] studied the welding of low-alloy high-strength steel. Their research demonstrated that a linear heat input had a significant impact on the tensile strength of weld joints. However, there exist few studies that focus on the mechanical properties of high-strength steel welded specimens under low-cycle fatigue loading. In particular, further experimental and theoretical studies on the mechanical properties of Q460 high-strength steel and different types of welded steel specimens under low-cycle fatigue loading are necessary.

In structural design using the high-strength steel, welded joints invariably exist in the steel material. However, the welded area is prone to high-strain low-cycle fatigue damage under the repeated action of loads. For example, the authors of this study simulated the mechanical behavior of Q460 steel columns under repeated seismic action. They observed that high-strength steel siding with high-strength steel column foot weld attachments was prone to fatigue damage and cracking, as illustrated in Figure 1. Therefore, to evaluate the mechanical performance of Q460 steel and its weld areas during earthquakes, it is necessary to perform repeated loading tests on this steel with welded joints.

To address the above problems, the following tasks were performed in the present investigation: (a) For the investigation under monotonic loading and repeated tension, 45 specimens of Q460 steel were prepared. The failure characteristics, stress-strain curves, skeleton curves, and energy consumption of the steel specimens with welded joints were analyzed. (b) The parameters affecting the mechanical properties of Q460 under repeated loading as well as their corresponding effects were analyzed. (c) Based on the experimental research and numerical simulation results, a design formula for the tensile strength of Q460 steel under repeated loading, which may provide a reference for its application in seismic engineering, was proposed.

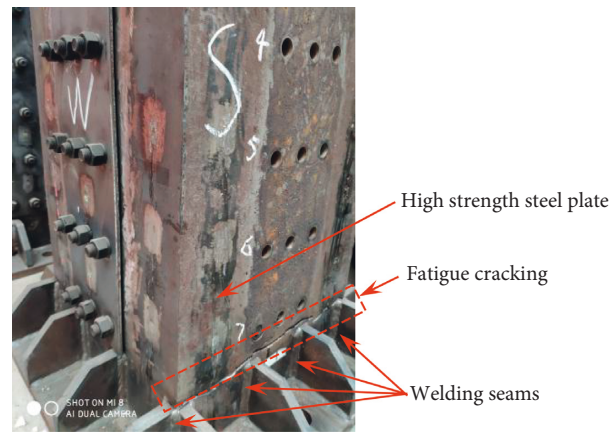

Figure 1: Fatigue cracking of the high-strength steel plate with welding seams under repeated loading.

2. Experimental Program

The Q460 steel used in this study was provided by Anshan Iron and Steel Group Corporation. The chemical composition of the steel, which meets the requirements of "High-strength low-alloy structural steels" (GB/T1591-2018, 2018) [15] is listed in Table 1. According to "Metallic materials tensile testing Part 1: Method of test at room temperature" (GB/T 228.1-2010, 2010) [16], Q460 plate specimens were prepared for cyclic tensile tests. The length and width of the clamping section of the plate specimen were 60 mm and 30 mm, respectively, and the radius of the curved transition section was 50 mm. The length and width of the parallel section were 53 mm and 12 mm, respectively. The welded joint was located on the middle axis of symmetry of the plate specimens. The design dimensions of the material specimen are depicted in Figure 2. The length and diameter of the clamping section of the rod specimen were 30 mm and 8 mm. The radius of the curved transition section was 30 mm.

We adopted the gas shielded welding method for welding. The specimens were divided into five groups, namely, A, B, C, D, and R. The welding consumable is ER80-d2 gas shielded welding wire. The heating temperature before welding was 50–60°C and the interlayer temperature was 80–100°C, which is suitable for welding low-alloy high-strength steels. The other welding parameters, which meet the requirements of the "Code for Welding of Steel Structures" (GB 50661-2011,2011) [17], are presented in Table 2.

Table 1: Chemical composition of Q460 (%).

C	Si	Mn	P	S	Cr	Al	Mo	Ti	Cu	Nb	Ni	V	Ceq
0.080	0.200	1.510	0.008	0.0013	0.050	0.030	0.003	0.002	0.070	0.021	0.030	0.045	358

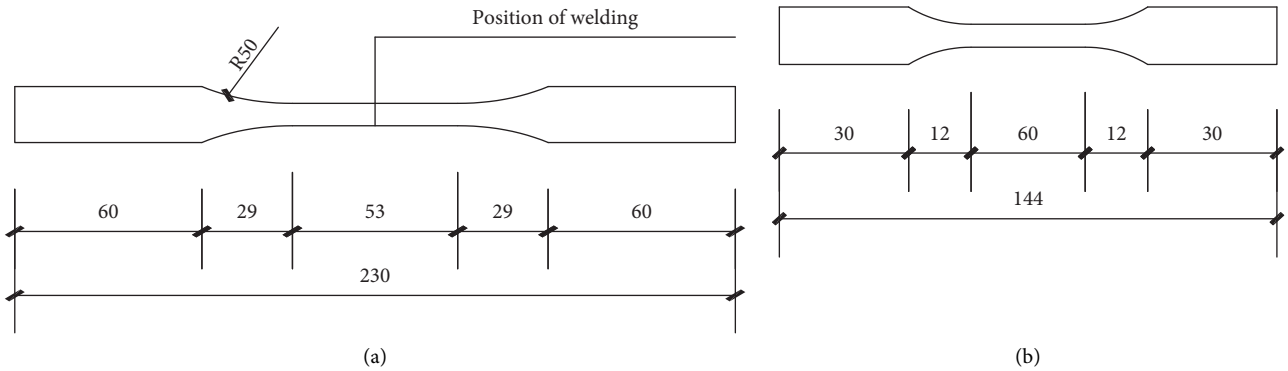

Figure 2: Specimen design (Units: mm). (a) Sheet material specimen. (b) Rod-shaped specimen.

Table 2: Welding parameters of Q460 submerged arc welding.

Welding method	Welding position and joint form	Welding current (A)	Welding voltage (V)	Welding Speed (cm/min)
CO2 gas shielded welding	Flat welding and board docking	220–280	24–28	30–35

The design parameters of the specimens are listed in Table 3. In the table, L and H represent the 12 mm and 6 mm thick plate specimens, respectively, whereas R represents the rod specimen with a diameter of 8 mm. The material tests were conducted on a CMT5105 electronic universal testing machine at Huaqiao University. The strain was measured by an extensometer with a gauge length of 50 mm and a range of 50%. The CMT5105 electronic universal testing machine and extensometer are produced and provided by MTS Industrial Systems (China) Co., Ltd.

The specimens were subjected to 16 loading patterns, including uniaxial tension loading and repeated tensile loading modes, as illustrated in Table 4. Specimens H/L-A-1, H/L-B-1, H/L-C-1, H/L-D-1, and R-A-1 were used for the uniaxial tensile tests, whereas the remaining specimens were used for the repeated tensile tests. Each test was carried out under displacement control with a loading speed of 0.6 mm/min.

3. Experimental Results and Discussion

3.1. Failure Mode. For the specimen without a welded joint, the fracture was located in the center of the middle parallel section. The necked section of the fracture demonstrated a considerable reduction in area and noticeable plastic deformation. Cracks in the specimen were generally distributed in a diamond shape, and fiber filaments were distributed on both sides of the fracture area. The failure mode I of the specimen is illustrated in Figure 3.

The failure modes of the material specimens with welded joints under uniaxial tension and those that were subjected to repeated tensile loading were different. Under uniaxial tension, microcracks first occurred in the specimen and then the crack developed continuously; microcracks developed into a large crack through the cross section. The specimen was easily broken in the heat-affected zone near the weld seam and the crack occurred on the part of the steel where it had a lower yield point. The cross section of the fracture was at an angle of 45° to the cross section of the specimen. The specimen exhibits slight necking when it breaks, as depicted in Figure 4(a). Failure Mode II was presented in specimens H/L-B-1, H/L-C-1, and H/L-D-1.

Under repeated tensile loading, lateral microcracks first appeared on the side of the welded joint specimen, and then the cracks continued to extend, developing along the lateral direction. For the specimen welded with Q460, the damage occurred in the middle weld position. For the specimens welding Q460 with Q235 or Q345 steel, the damage occurred near the weld area and close to the side of the steel plate with lower yield strength. Necking was not observed when the specimen was broken. A specimen with a welded joint subjected to repeated tension exhibiting Failure Mode III is depicted in Figure 4(b).

3.2. Material Properties. To study the effects of the design dimensions, connection method, and loading mechanism on the material properties of specimens, the stress-strain curves of the specimens were compared and analyzed. The strain of the specimen in the stress-strain curve was measured using the extensometer, and the stress in the curve represented the cross-sectional stress of the specimen.

The test results for the Q460 steel specimens after single tension and repeated loading are summarized in Table 5. Here, E is the elastic modulus of the specimen; f_y and f_u are the yield stress and maximum tensile stress of the steel, respectively; ε_u is the strain corresponding to the maximum tensile stress f_u; ε is the strain when the tensile strength drops

Table 3: Specimen description.

Specimen label	Welding condition	Thicknesst t (mm)	Loadingpatterns	Specimen label	Welding condition	Thicknesst t (mm)	Loadingpatterns
H-A-1	No welding	6	NM1	L-C-1	Welded with Q235 steel	12	NM1
H-A-2	No welding	6	NM2	L-C-9	Welded with Q235 steel	12	NM9
H-A-3	No welding	6	NM3	L-C-10	Welded with Q235 steel	12	NM10
H-A-4	No welding	6	NM4	L-C-11	Welded with Q235 steel	12	NM11
H-A-5	No welding	6	NM5	L-C-12	Welded with Q235 steel	12	NM12
L-A-1	No welding	12	NM1	L-C-13	Welded with Q235 steel	12	NM13
L-A-2	No welding	12	NM2	H-D-1	Welded with Q345 steel	6	NM1
L-A-3	No welding	12	NM3	H-D-9	Welded with Q345 steel	6	NM9
L-A-4	No welding	12	NM4	H-D-10	Welded with Q345 steel	6	NM10
L-A-5	No welding	12	NM5	H-D-11	Welded with Q345 steel	6	NM11
H-B-1	Welded with Q460 steel	6	NM1	H-D-12	Welded with Q345 steel	6	NM12
H-B-7	Welded with Q460 steel	6	NM7	H-D-13	Welded with Q345 steel	6	NM13
H-B-8	Welded with Q460 steel	6	NM8	L-D-1	Welded with Q345 steel	12	NM1
L-B-1	Welded with Q460 steel	12	NM1	L-D-9	Welded with Q345 steel	12	NM9
L-B-14	Welded with Q460 steel	12	NM14	L-D-10	Welded with Q345 steel	12	NM10
L-B-15	Welded with Q460 steel	12	NM15	L-D-11	Welded with Q345 steel	12	NM11
L-B-16	Welded with Q460 steel	12	NM16	L-D-12	Welded with Q345 steel	12	NM12
H-C-1	Welded with Q235 steel	6	NM1	L-D-13	Welded with Q345 steel	12	NM13
H-C-9	Welded with Q235 steel	6	NM9	R-A-1	No welding	8	NM1
H-C-10	Welded with Q235 steel	6	NM10	R-A-3	No welding	8	NM3
H-C-11	Welded with Q235 steel	6	NM11	R-A-4	No welding	8	NM4
H-C-12	Welded with Q235 steel	6	NM12	R-A-5	No welding	8	NM5
H-C-13	Welded with Q235 steel	6	NM13	R-A-6	No welding	8	NM6

by 15%; fy/fu is the yield ratio; W is the elongation; Em is the hysteresis energy; and n is the number of loading cycles. L and H represent 12 mm and 6 mm thick plate specimens, respectively, and R represents rod specimens with a diameter of 8mm. According to the welding conditions, it is divided into four groups: A, B, C, and D. The third digit of "H-A-1" corresponds to the loading pattern.

3.2.1. Effect of Specimen Thickness. The stress-strain curves for plate specimens with thicknesses of 6 mm and 12 mm were measured under the NM1, NM4, and NM11 loading modes, as depicted in Figure 5(a). The analysis of Figure 5(a) and Table 3 shows that there is an obvious difference in the ultimate tensile strength of the specimens with different thicknesses. By analyzing the ultimate tensile strength of the specimens of groups A and C, it was found that the ultimate tensile strength of the 12-mm-thick specimen was greater than that of the 6-mm-thick specimen. The stress-strain curve for the specimens indicated that specimens without welded joints experienced the elastic stage, plastic stage, strengthening stage, and a yield stage was also evident. The results indicate that the thickness of the specimens has a significant effect on the ductility of the steel and an increase

Table 4: Loading patterns of tested specimens.

Loading pattern	Instructions
NM1	Unidirectional tensile loading speed 0.6 mm/min loading until the specimen fracture
NM2	Repeated tensile loading mode, loading speed 0.6 mm/min, and loading strain 9%, equal amplitude loading. In each loading cycle, unloading after loading to the maximum strain. The specimen is directly pulled and broken after nine turns of cyclic loading
NM3	Repeated tensile loading mode, loading speed 0.6 mm/min, and loading strain 3%, 5%, 7%, 8%, and 9%. In each loading cycle, unloading after loading to the maximum strain, each stage is loaded in a cycle of one turn, and the final stage is loaded in a cycle of three turns, after which the loading continues until the specimen breaks.
NM4	Repeated tensile loading mode, loading speed 0.6 mm/min, and loading strain 3%, 5%, 7%, 8%, and 9%. In each loading cycle, unloading after loading to the maximum strain. Each stage is loaded in a cycle of two turns, and the final stage is loaded in a cycle of four turns, after which the loading continues until the specimen breaks
NM5	Repeated tensile loading mode, loading speed 0.6 mm/min, and loading strain 3%, 4%, 5%, 6%, 7%, 8%, and 9%. In each loading cycle, unloading after loading to the maximum strain, each stage is loaded in a cycle of one turn, and the final stage is loaded in a cycle of three turns, after which the loading continues until the specimen breaks
NM6	Repeated tensile loading mode, loading speed 0.6 mm/min, and loading strain 3%, 4%, 5%, 6%, 7%, 8%, and 9%. In each loading cycle, unloading after loading to the maximum strain, each stage is loaded in a cycle of two turns, and the final stage is loaded in a cycle of four turns, after which the loading continues until the specimen breaks
NM7	Repeated tensile loading mode, loading speed 0.6 mm/min, loading strain 1.5%, and equal width loading. In each loading cycle, unloading after loading to the maximum strain, the specimen is directly pulled and broken after nine turns of cyclic loading
NM8	Repeated tensile loading mode, loading speed 0.6 mm/min, and loading strain 0.5%, 1%, 1.5%, 2%, 2.5%, and 3%. In each loading cycle, unloading after loading to the maximum strain, each stage is loaded in a cycle of one turn, and the final stage is loaded in a cycle of three turns, after which the loading continues until the specimen breaks
NM9	Repeated tensile loading mode, loading speed 0.6 mm/min, loading strain 4%, and equal amplitude loading. In each loading cycle, unloading after loading to the maximum strain. The specimen is directly pulled and broken after nine turns of cyclic loading
NM10	Repeated tensile loading mode, loading speed 0.6 mm/min, and loading strain 1%, 2%, 3%, 4%, and 5%. In each loading cycle, unloading after loading to the maximum strain, each stage is loaded in a cycle of one turn, and the final stage is loaded in a cycle of three turns, after which the loading continues until the specimen breaks
NM11	Repeated tensile loading mode, loading speed 0.6 mm/min, and loading strain 1%, 2%, 3%, 4%, and 5%. In each loading cycle, unloading after loading to the maximum strain, each stage is loaded in a cycle of two turns, and the final stage is loaded in a cycle of four turns, after which the loading continues until the specimen breaks
NM12	Repeated tensile loading mode, loading speed 0.6 mm/min, and loading strain 0.5%, 1%, 1.5%, 2%, 2.5% ... 5%. In each loading cycle, unloading after loading to the maximum strain, each stage is loaded in a cycle of one turn, and the final stage is loaded in a cycle of three turns, after which the loading continues until the specimen breaks
NM13	Repeated tensile loading mode, loading speed 0.6 mm/min, loading strain 0.5%, 1%, 1.5%, 2%, 2.5% ... 5%. In each loading cycle, unloading after loading to the maximum strain, each stage is loaded in a cycle of two turns, and the final stage is loaded in a cycle of four turns, after which the loading continues until the specimen breaks
NM14	Repeated tensile loading mode, loading speed 0.6 mm/min, loading strain 2%, and equal amplitude loading. In each loading cycle, unloading after loading to the maximum strain. The specimen is directly pulled and broken after nine turns of cyclic loading
NM15	Repeated tensile loading mode, loading speed 0.6 mm/min, loading strain 0.5%, 1%, 1.5%, and 2%. In each loading cycle, unloading after loading to the maximum strain, each stage is loaded in a cycle of one turn, and the final stage is loaded in a cycle of three turns, after which the loading continues until the specimen breaks
NM16	Repeated tensile loading mode, loading speed 0.6 mm/min, and loading strain 0.5%, 1%, 1.5%, and 2%. In each loading cycle, unloading after loading to the maximum strain, each stage is loaded in a cycle of two turns, and the final stage is loaded in a cycle of four turns, after which the loading continues until the specimen breaks

in thickness is beneficial to the ductility. In addition, specimens with welded joints did not exhibit an obvious yield stage.

The stress-strain curves of the plate specimens with a thickness of 6 mm and the rod specimen with a diameter of 8 mm under the three loading modes of NM1, NM3, and NM4 are illustrated in Figure 5(b). For the same loading mode, the ultimate tensile strength of the rod specimen was considerably higher than that of the plate specimen, and its ductility was lesser than that of the plate specimen. Furthermore, the stress degradation rate of the rod specimen was faster after reaching its ultimate tensile strength.

3.2.2. Effect of Welding Connection. The stress-strain curves of the plate specimens of groups A–D are illustrated in Figure 6. Figure 6(a) shows that under uniaxial tension, the group A specimen has a more obvious yield stage. In contrast, the tested specimens of groups B, C, and D have no evident yield stages. The test curve of the Group A specimen is plump, and the ductility and tensile strength of group A specimens are greater than those of groups B, C, and D. The tensile strength of the group C specimens is higher than that of the group D specimens while its ductility is lower. This implies that when the specimen was welded with Q460, its strength and ductility are enhanced, but its tensile strength is

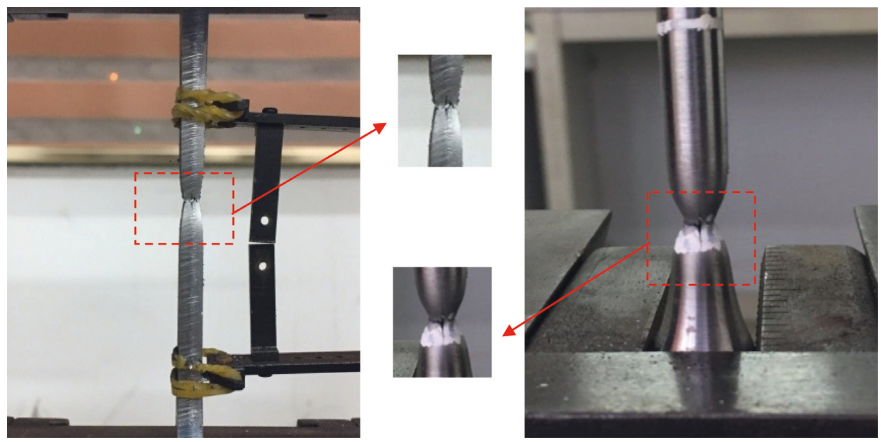

(a) (b)

Figure 3: Failure mode I of specimens without welded joint. (a) Sheet material specimen. (b) Rod-shaped specimen.

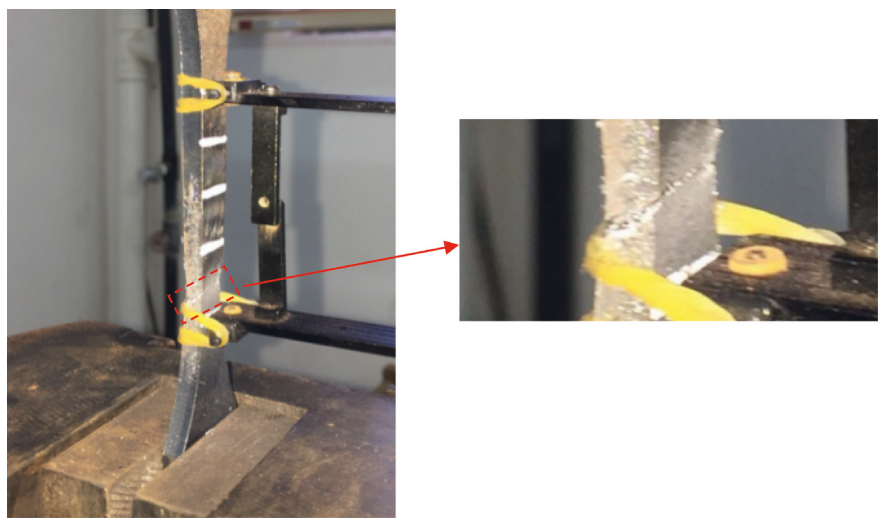

(a)

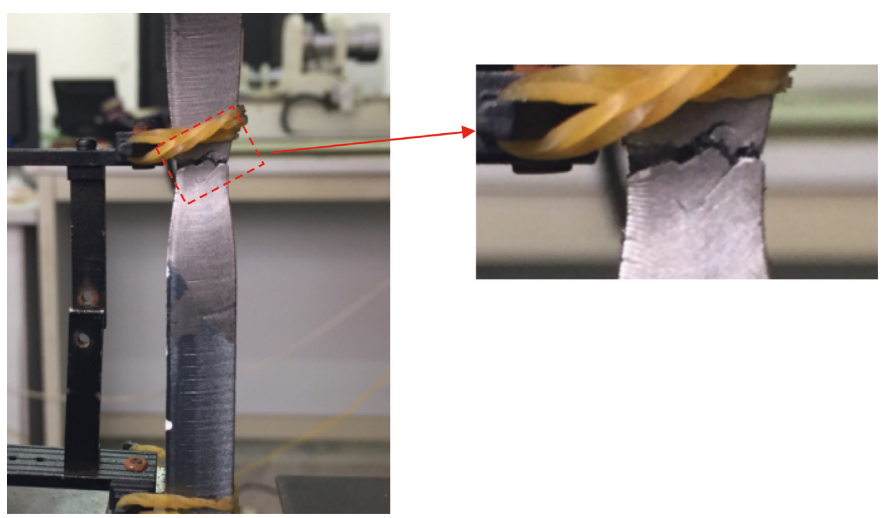

(b)

Figure 4: (a) Failure mode II of specimens with welded joint. (b) Failure mode III of specimens with welded joint.

Table 5: Summary of test results.

Specimen label	E (×105 MPa)	f_y (MPa)	f_u (MPa)	ε_u	ε	f_y/f_u	W (%)	E_m (J)	n (cycles)	Failure mode
H-A-1	2.11	549	626	11.00	18.94	0.62	22.40	444	1	I
H-B-1	1.97	480	509	1.59	2.32	0.71	4.00	49	1	II
H-C-1	2.00	321	462	5.09	9.86	0.68	14.00	154	1	II
H-D-1	1.92	280	419	6.38	13.45	0.64	16.00	199	1	II
H-A-2	2.14	548	632	12.00	19.72	0.62	27.00	476	9	I
H-B-7	1.94	510	603	5.02	6.52	0.54	10.00	145	9	III
H-C-9	2.23	316	452	3.81	5.73	0.65	16.00	74	9	III
H-D-9	2.11	368	414	6.14	12.98	0.65	18.00	200	9	III
H-A-3	2.16	550	625	11.95	18.89	0.60	25.60	445	6	I
H-B-8	1.96	450	560	2.67	3.74	0.57	6.00	87	8	III
H-C-10	2.24	303	443	4.67	4.63	0.67	14.00	66	7	III
H-D-10	2.14	370	414	5.46	11.78	0.65	15.00	179	7	III
H-C-11	2.13	305	452	5.30	10.68	0.66	15.00	158	12	III
H-D-11	2.13	385	423	6.22	13.09	0.67	17.00	208	12	III
H-A-4	2.17	546	613	11.19	18.82	0.61	26.60	447	9	I
H-C-12	2.13	321	460	5.04	8.94	0.69	12.70	142	11	III
H-D-12	2.14	373	417	6.73	13.73	0.66	17.00	213	11	III
H-C-13	2.18	301	451	4.34	10.81	0.67	14.00	162	20	III
H-D-13	2.23	368	406	6.74	13.85	0.66	18.00	213	20	III
L-A-1	2.11	556	683	18.83	28.21	0.45	29.60	1226	1	I
L-B-1	2.29	479	601	1.98	3.45	0.63	7.00	174	1	II
L-C-1	2.08	382	450	5.74	10.05	0.63	16.00	306	1	II
L-D-1	2.25	426	520	7.06	14.83	0.44	22.00	606	1	II
L-A-2	2.18	515	708	8.73	16.18	0.59	24.40	939	9	I
L-B-14	1.84	350	564	2.15	2.88	0.62	6.00	143	9	III
L-C-9	2.05	315	456	6.08	11.78	0.63	14.40	353	9	III
L-D-9	1.88	350	529	6.70	13.14	0.67	18.00	525	9	III
L-A-3	2.20	551	701	8.54	17.42	0.64	24.00	954	6	I
L-B-15	1.90	316	581	1.52	2.83	0.54	7.10	124	6	III
L-C-10	2.30	329	446	6.44	12.46	0.65	14.00	354	7	III
L-D-10	2.03	363	567	5.29	11.79	0.64	17.60	505	7	III
L-A-4	2.34	543	712	8.82	19.43	0.62	26.00	1096	10	I
L-B-16	1.89	342	614	2.00	2.32	0.56	4.80	146	10	III
L-C-11	2.31	369	445	6.50	11.50	0.61	13.60	333	12	III
L-D-11	1.96	333	545	4.53	9.52	0.61	16.00	411	12	III
L-C-12	1.82	373	454	5.92	11.37	0.60	16.00	351	11	III
L-D-12	2.17	351	545	4.88	12.04	0.65	18.00	538	11	III
L-C-13	2.01	402	449	5.51	9.47	0.67	12.40	288	20	III
L-D-13	2.16	353	549	5.26	12.64	0.64	16.00	544	20	III
R-A-1	2.30	550	742	11.39	17.16	0.61	20.00	334	1	I
R-A-3	2.05	554	721	9.93	16.85	0.55	22.00	334	6	I
R-A-4	2.04	561	714	10.04	14.74	0.56	21.50	292	10	I
R-A-5	1.95	563	698	9.67	12.72	0.56	16.00	243	9	I
R-A-6	1.96	573	737	9.72	17.90	0.55	24.00	358	16	I

reduced. Group B specimens first reach their ultimate tensile strength and cracking occurs rapidly after reaching the peak strength. This is because of the numerous initial defects caused by the welding process. Therefore, the welding process and the properties of the welding consumable have a major influence on the test results. The stress-strain curves of the tested specimens of groups C and D with different thicknesses are depicted in Figure 6(b). For the 6-mm-thick specimen, the ultimate tensile strength of the group C specimens is higher than that of the group D specimens; however, the ductility is lower. For the 12-mm-thick specimens, the tensile strength and ductility of the group D specimens are higher than those of the group C specimens. The stress-strain curve of the group D specimens is plumper and the energy-consumption capability is greater than that of the group C specimens. These results indicate that the thickness of the specimens and the strength of the welding steel affect the mechanical properties of the welded specimens. Welding reduces the ductility of the specimen to a certain extent, which is not conducive to the development of the plasticity stage of the specimen. The closer the strength of the welded steel plate to that of the base material, the better the mechanical properties of the welded specimens.

3.2.3. Effect of Loading Patterns. The stress-strain curve and the yield ratio of the three groups of specimens, that is, R-A, L-C, and H-D, in different loading modes are depicted in

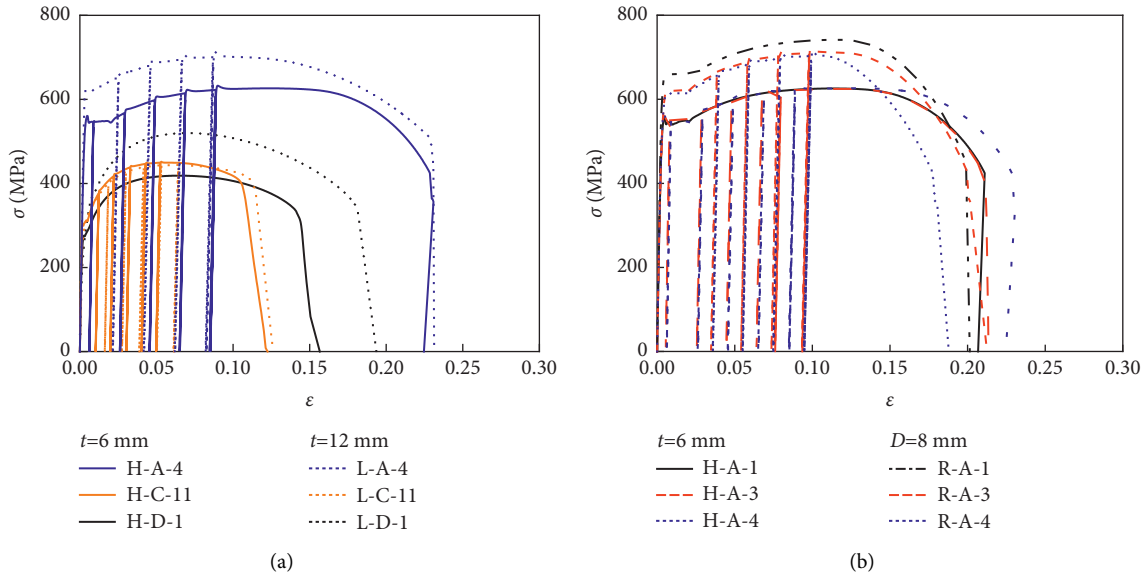

FIGURE 5: Stress-strain curves of material specimens. (a) Material specimens with different thicknesses. (b) Material specimens with different cross section shapes.

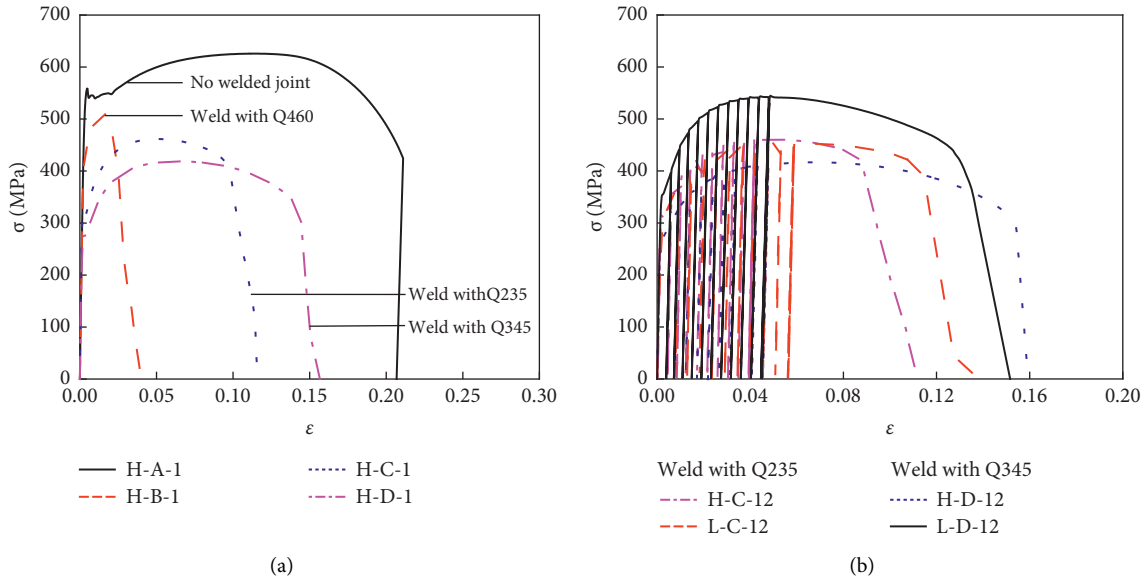

FIGURE 6: Stress-strain curves of welded material specimens with different material strengths. (a) Material specimens in the NM1 loading pattern. (b) Material specimens in the NM12 loading pattern.

Figure 7. Group R-A consists of rod specimens without welded joints. As depicted in Figure 7(a), the specimens exhibit an obvious yield stage. The R-A specimens exhibit significant strength hardening and good ductility. Their stress-strain curves are plump in shape, indicating their strong ability of energy dissipation. Group L-C comprises the plate specimens welded with Q460 and Q235 steels. As illustrated in Figure 7(b), under repeated loading, the variation in the tensile strength of the specimen is not readily evident, but the ductility decreases. The specimen L-C-13 enters the failure stage prematurely. This is primarily because the grade of the welded steel material is different with that of the other groups, resulting in considerable plastic damage under repeated loading. Consequently, the mechanical properties of the specimen decrease and the specimens are rapidly destroyed. The H-D group is composed of a plate specimen with welded Q460 and Q345 steels. As depicted in Figure 7(c), with the increase in the number of loading cycles, the ductility and energy-consumption capacity of the specimens are enhanced, and the change of their tensile strength is not very evident. It can be observed from Figure 7(d) that the loading mode has less influence on the yield ratio of the material specimen. These results indicate that as the number of cyclic loadings increases, the impact on the mechanical properties of the specimen is more significant. In addition, when the number of loading cycles is

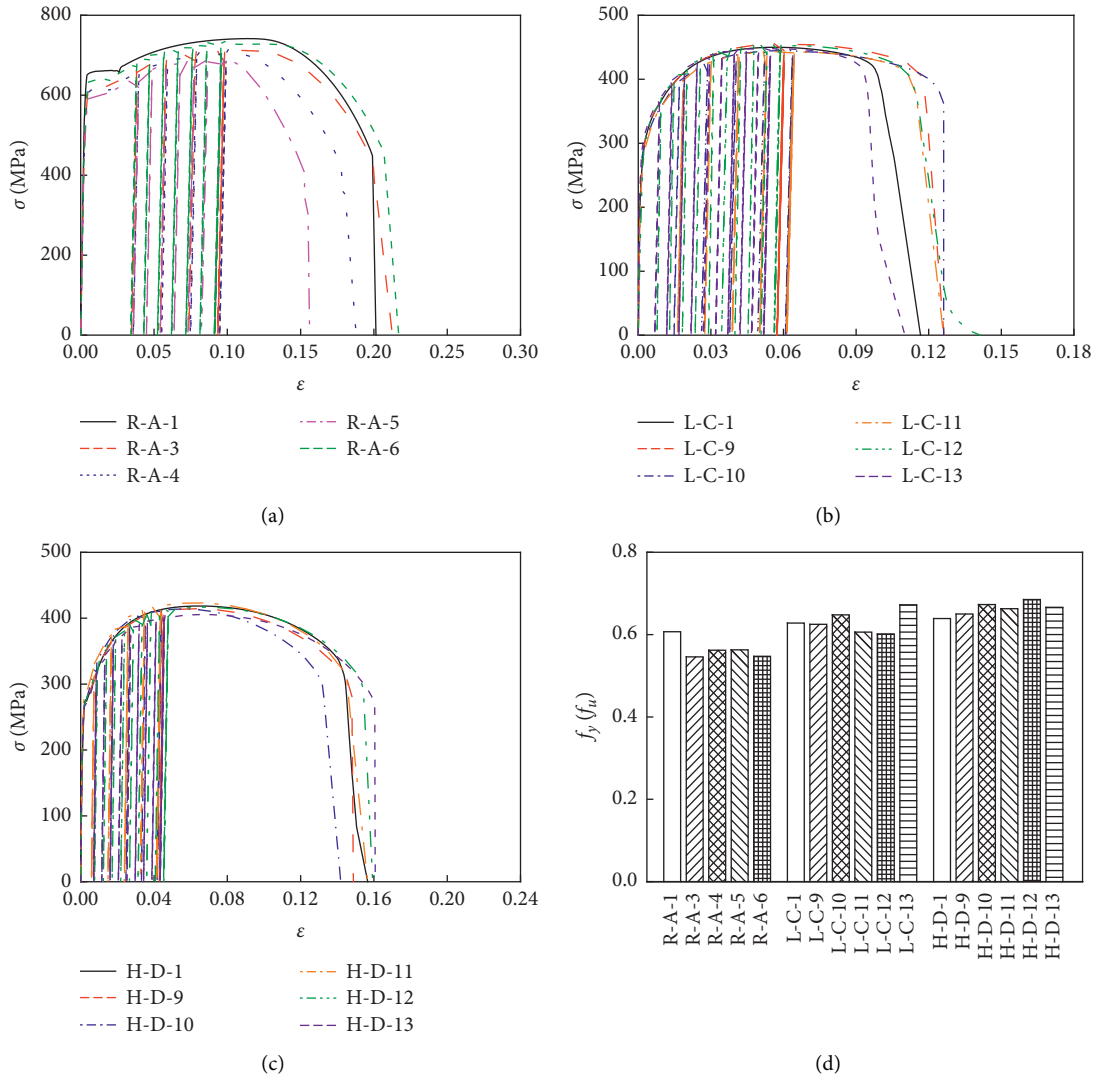

Figure 7: Effect of different loading patterns on stress-strain curves of specimens. (a) Specimens of group R-A. (b) Specimens of group L-C. (c) Specimens of group H-D. (d) The ratio of yield strength to ultimate tensile strength of three sets of specimens in different loading modes: R-A, L-C, and H-D.

small, the influences of the number of cycles and the maximum strain amplitude on the yield ratio of the specimen are not significant.

3.3. Hysteresis Behavior. The energy dissipation capacity *Em* [18] of the specimen can be measured by the area surrounded by the load-displacement curve or stress-strain curve. Figure 8 describes the hysteretic properties of specimens with different thicknesses. Analysis of Figures 8(a) and 8(b) shows that the energy dissipation capacity of the specimen with 12 mm thickness is better than that of the specimen with 6 mm thickness. The ultimate tensile strength of 12 mm thick material specimens is higher than that of 6 mm thick material specimens. The experimental results show that the thickness of the material specimen has a great influence on the energy dissipation capacity of the specimen, and the specimen with a larger cross section thickness has better energy dissipation capacity than the specimen with a smaller cross section thickness.

Figure 9 depicts a comparison of the hysteretic energy values of specimens of groups A, C, and D under uniaxial tension. The energy consumption of the group A specimens without a welded joint is better than that of other specimens with a welded joint. The energy consumption of the group D specimens is better than that of the group C specimens. This finding indicates that the welded joint reduces the energy consumption of the specimen to a certain extent. In addition, the energy consumption of the specimens with welded joints increases with the increase in the strength of the welded steel.

The hysteretic energy plots for the H-D and L-D specimens are depicted in Figure 10. The energy consumptions of the H-D and L-D specimens increase with the number of loading cycles. In loading modes NM10, NM9, and NM12, the energy consumptions of the specimens improve

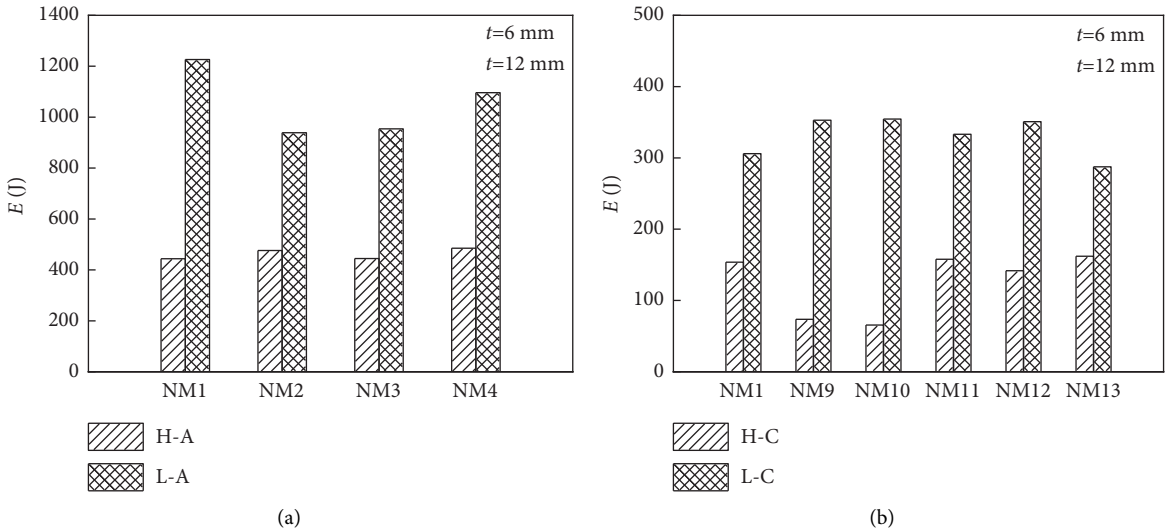

Figure 8: Hysteresis energy of specimens with different welding steel. (a) Hysteresis energy of specimens with label A. (b) Hysteresis energy of specimens with label C.

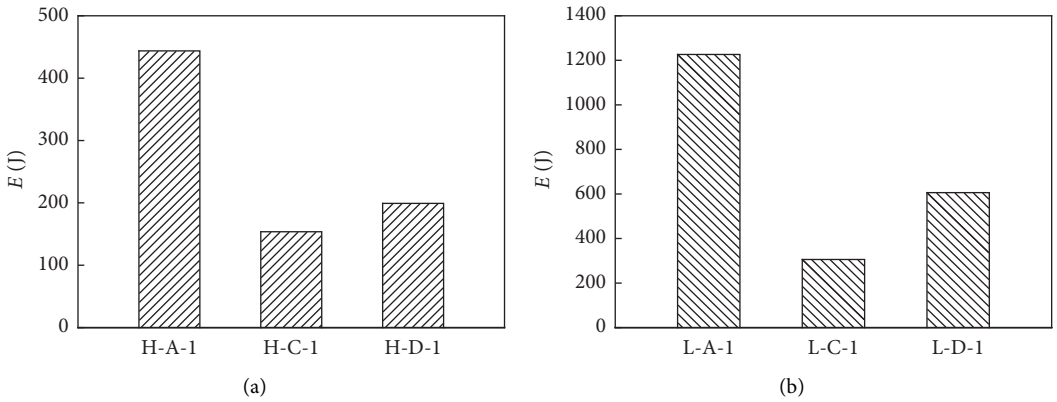

Figure 9: Hysteresis energy of specimens with different thickness. (a) Hysteresis energy of specimens with 6 mm thickness. (b) Hysteresis energy of specimens with 12 mm thickness.

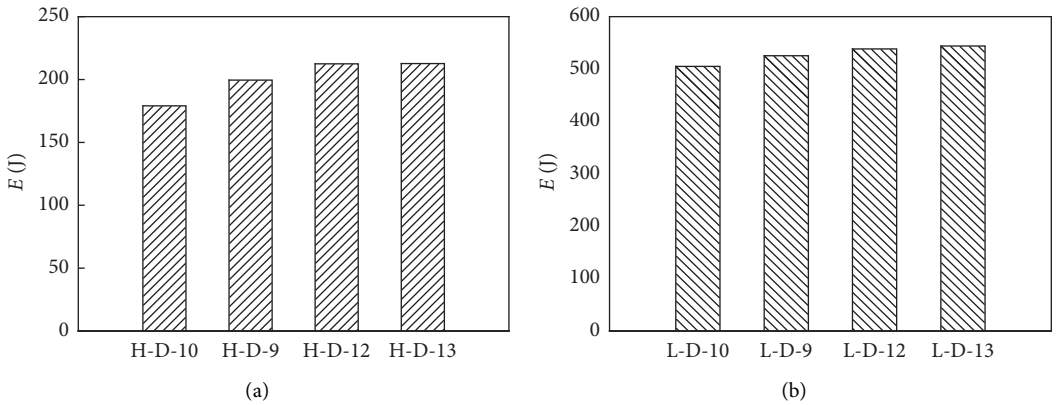

Figure 10: Hysteresis energy of material specimens under different thickness and loading modes. (a) Hysteresis energy of specimens with label H-D. (b) Hysteresis energy of specimens with label L-D.

substantially. However, under loading modes NM12 and NM13, the improvement in the energy consumption of the specimen is no longer evident. Thus, the energy-consumption capacity of the specimen increases substantially with the increase in the number of cycles. Nevertheless, after reaching a certain number of cycles, no significant improvement in the energy consumption can be observed.

3.4. Skeleton Curves. The skeleton curves for the specimens of groups H and R are depicted in Figure 11(a). The analysis of Figure 11(a) reveals that the initial stiffness and strength of the group H specimens are greater than those of the group R specimens. The bearing capacity of the group H specimens in the late loading stage is lesser than that of the group R specimens. This indicates that the stiffness and strength of the plate specimens are higher than those of the rod specimens in the initial loading stage. In the later stages of repeated loading, the load-bearing capacity of the plate specimen becomes smaller than that of the rod specimen, but its ductility is superior.

Figure 11(b) depicts a comparison of the skeleton curves of the specimens with different thicknesses. The strength and rigidity of the group L-D specimens are significantly higher than those of the group H-D specimens. This implies that the increase in thickness of the specimens has a significant influence on their strength and stiffness. However, the loading mode has no major effect on their stiffness.

The skeleton curves for the 6-mm-thick specimens of groups C and D with welded joints are illustrated in Figure 11(c). With an increase in the number of loading cycles, the group C specimens possess higher stiffness than that of the group D specimens. However, the strength of the group D specimens is higher. This indicates that the strength of the welding material has a significant influence on the strength and rigidity of the specimen. The closer the strength of the welding material is to that of the base material, the higher the stiffness and strength of the specimen.

4. Finite Element Analysis

4.1. Finite Element Model. A finite element model of the specimen with the design parameters of the Q460 steel was established through the ANSYS program, as depicted in Figure 12(a) Through comprehensive consideration of the calculation speed, calculation accuracy, postprocessing results, and simulation phenomenon display, the finite element model used an 8-node hexahedral solid element SOLID 185. To facilitate convergence of the calculation results, the specimen was divided using an element size of 2 mm as the control parameter, and the finite element mesh was close to a square. The node displacement corresponding to the test loading strain was applied through the upper clamped section, while the consolidation constraint was applied via the lower clamped section. The multilinear follow-up strengthening model, KINH, was selected, and the constitutive relationship of the Q460 steel in the finite element model was defined by referring to the experimentally measured stress-strain curve of the Q460 steel specimen, as depicted in Figure 12(b). Strain stretching was used to control the strain amplitude of the finite element model. Similar to the experimental study, when the tensile strength of the finite element model drops by 15%, it is considered that the model has undergone low-cycle fatigue failure [19]. It is worth noting that the finite element simulation part does not consider the impact of welding.

4.2. Verification of the Finite Element Model. The failure morphology comparison between the experimental test and finite element simulation results of the specimen L-A-3 are depicted in Figure 13. In Figure 13(b), it can be seen that the model exhibits necking behavior. The actual deformation form in the middle tensile section of the specimen is consistent with the finite element simulation. In addition, the finite element model can simulate the necking behavior of the specimens under tensile failure. This implies that the finite element model can accurately simulate the deformation characteristics of the Q460 steel specimens.

To further verify the accuracy of the finite element model in the same loading mode as the experimental study, the stress-strain curves of three groups of specimens, namely, L-A-2, H-A-3, and H-A-5, were compared. As illustrated in Figure 14, the strength, stiffness, and envelope area of the finite element simulation curve and the test curve agree well. This indicates that the finite element model established in this study has high calculation accuracy. Q460 steel could exhibit both kinematic and isotropic hardening characteristics under cyclic loading, and therefore it is anticipated that a combined kinematic/isotropic hardening model may adequately capture its fundamental hysteretic behaviour [20].

4.3. Parametric Study. To further investigate the influence of the length of the parallel tensile zone of the specimen, the thickness of the specimen, the shape of the cross section, and loading mechanism on the mechanical properties of the Q460 steel specimen, 38 numerical simulation specimens were designed. The designed parameters are detailed in Table 6, where P and R represent specimens in a sheet shape and a rod shape, respectively, and M represents the simulation model. The loading patterns of the numerical simulation specimen are illustrated in Figure 15.

To investigate the influence of the specimen dimensions on the mechanical properties of the specimens, hysteresis curves for the Q460 specimens with different dimensions and cross-sectional shapes, under the repeated loading mode NM19, were extracted. The abscissa ε represents the average strain of the intermediate tension section, and the ordinate σ represents the average stress of the cross section of the intermediate tension section.

The hysteresis curves of the test specimens with tension zones of different lengths are plotted in Figure 16. The test curves of specimens P-M-1 and R-M-1 are plumper than those of corresponding groups of specimens, and the degradation behavior is not obvious. This indicates that when the length of the tension zone is small, the hysteresis curve of the specimen is plumper and the degradation of the curve in the later stages of the loading cycle is more gradual. When

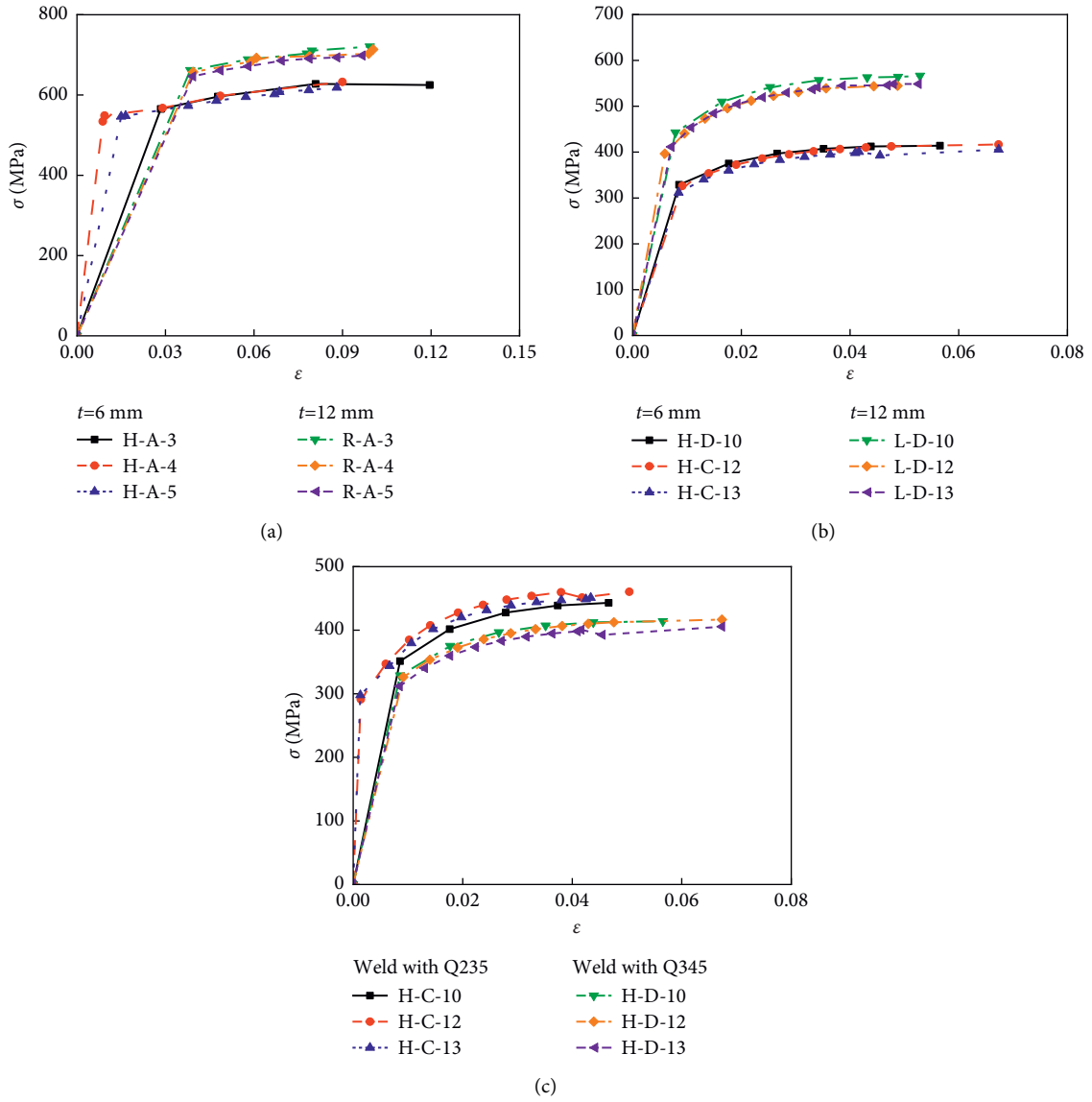

Figure 11: Skeleton curves of specimens. (a) Skeleton curves of specimens without welded joint. (b) Skeleton curves of material specimens with different thickness. (c) Skeleton curves of material specimens with different material strength of the plate.

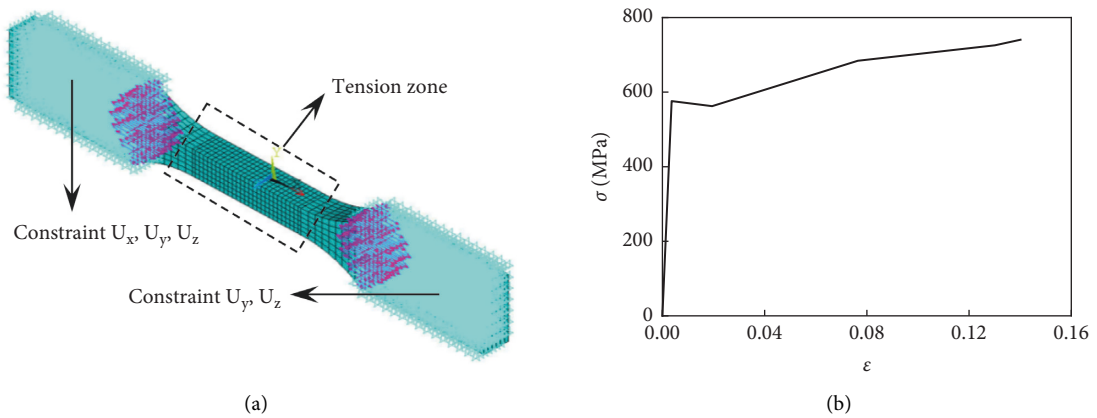

Figure 12: Configuration of the finite element model of the tested specimen. (a) Finite element mode. (b) Constitutive relationship of material.

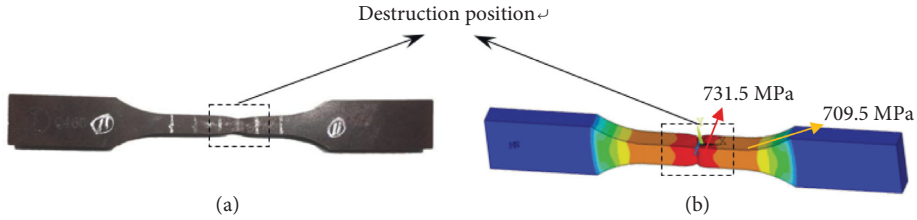

Figure 13: Results comparison of specimen L-A-3. (a) Failure pattern in the experimental test. (b) Failure pattern in finite element simulation.

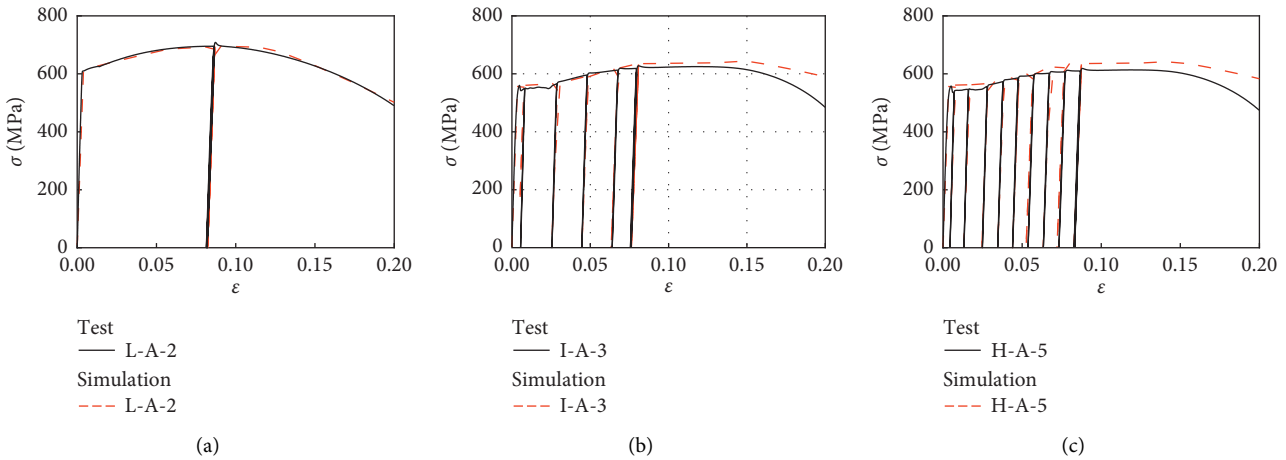

Figure 14: Comparison of stress-strain curves. (a) Specimen L-A-2. (b) Specimen H-A-3. (c) Specimen H-A-5.

Table 6: Summary of dimensions of specimens in simulation models.

Specimen label	Parallel length L (mm)	Thickness t (mm)	Loading patterns
P-M-1	30	10	NM19
P-M-2	35	10	NM19
P-M-3	40	10	NM19
P-M-4	45	10	NM19
P-M-5	50	10	NM19
P-M-6	55	10	NM19
P-M-7	60	10	NM19
P-M-8	50	5	NM19
P-M-9	50	7.5	NM19
P-M-10	50	12.5	NM19
P-M-11	50	15	NM19
P-M-12	50	10	NM17
P-M-13	50	10	NM18
P-M-14	50	10	NM20
P-M-15	50	10	NM21
P-M-16	50	10	NM22
P-M-17	50	10	NM23
P-M-18	50	10	NM24
P-M-19	50	10	NM25
R-M-1	30	14	NM19
R-M-2	35	14	NM19
R-M-3	40	14	NM19
R-M-4	45	14	NM19
R-M-5	50	14	NM19
R-M-6	55	14	NM19
R-M-7	60	14	NM19
R-M-8	50	10	NM19
R-M-9	50	12	NM19

Table 6: Continued.

Specimen label	Parallel length L (mm)	Thickness t (mm)	Loading patterns
R-M-10	50	15.5	NM19
R-M-11	50	17	NM19
R-M-12	50	14	NM17
R-M-13	50	14	NM18
R-M-14	50	14	NM20
R-M-15	50	14	NM21
R-M-16	50	14	NM22
R-M-17	50	14	NM23
R-M-18	50	14	NM24
R-M-19	50	14	NM25

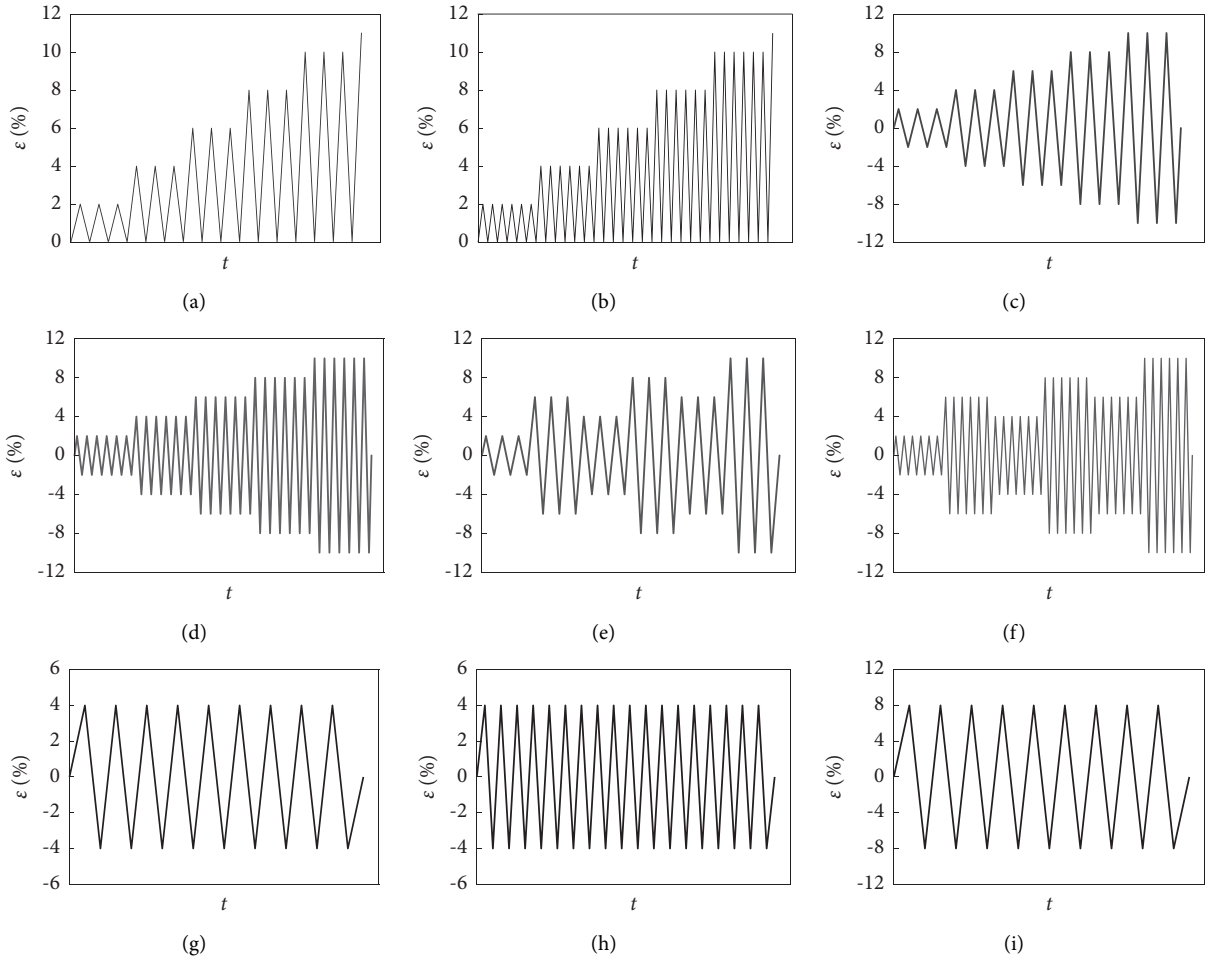

Figure 15: Loading patterns of the numerical simulation specimens (s). (a) Loading pattern NM17. (b) Loading pattern NM18. (c) Loading pattern NM19. (d) Loading pattern NM20. (e) Loading pattern NM21. (f) Loading pattern NM22. (g) Loading pattern NM23. (h) Loading pattern NM24. (i) Loading pattern NM25.

the length of the tension zone of the specimen is large, the area of the hysteresis loop is small and the degradation of the curve in the later stages of loading is more evident.

The hysteresis curves of the plate specimens with different thicknesses and rod specimens with different diameters were evaluated. As illustrated in Figure 17, for specimens P-M-11 and R-M-5, which have large cross-sectional dimensions, the hysteresis curve is broader, and during the later stages of loading, the curve degrades more gradually. This result indicates that the cross-sectional area affects the energy consumption of Q460. As the cross-sectional area of the specimen increases, its energy consumption and plastic deformation capability also increase.

The hysteresis curves for specimens with different cross-sectional areas were plotted. As depicted in Figure 18, the hysteresis curve of the group P plate specimens is plumper

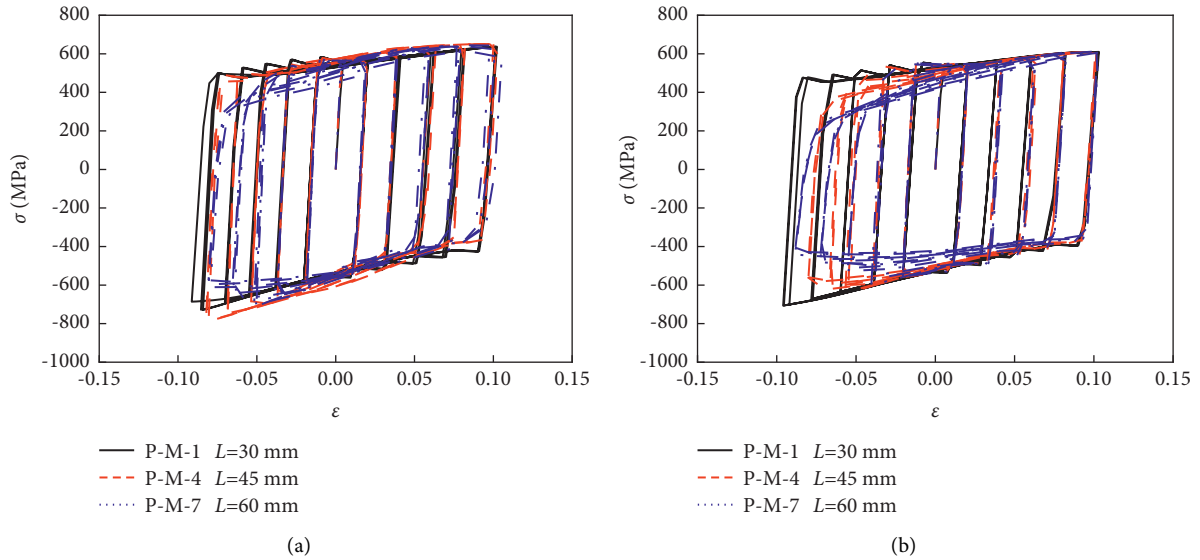

Figure 16: Hysteresis curves of material specimens with different parallel lengths. (a) Hysteresis curves of specimens in group P-M. (b) Hysteresis curves of specimens in group R-M.

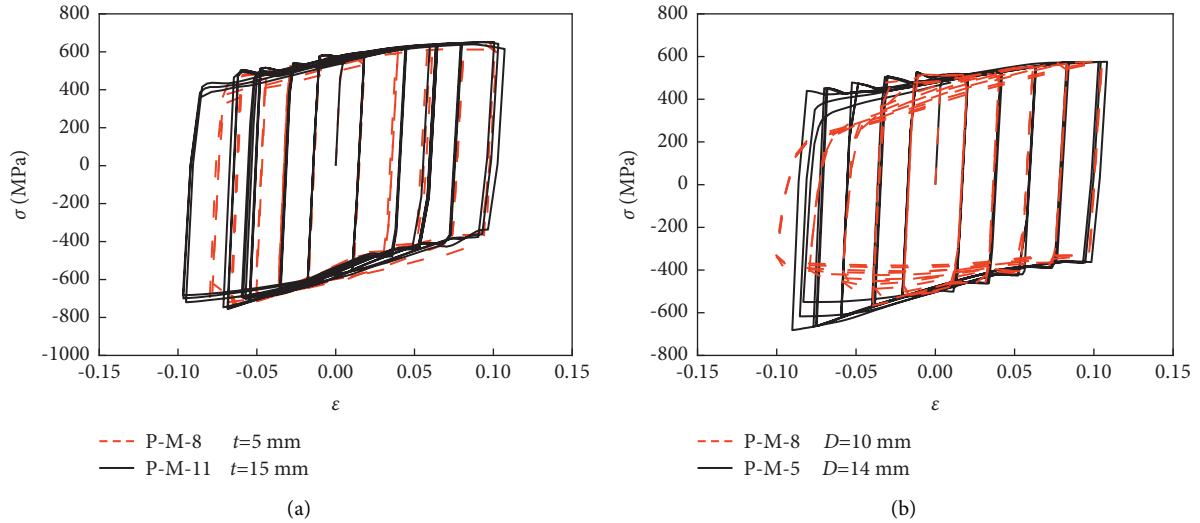

Figure 17: Hysteresis curves of material specimens with different thickness or diameter. (a) Hysteresis curves of specimens in group P-M. (b) Hysteresis curves of specimens in group R-M.

than that of the group R rod specimens, and degradation of the hysteresis curve is more gradual during the later stages of loading. This indicates that for the same cross-sectional area and loading mode, the hysteresis curve of the plate specimen is broader than that of the rod specimen of the same material. The plate specimen also exhibits better plastic deformation capability during the later stages of loading.

4.4. Effect of Various Parameters

4.4.1. Influence of the Length of the Tension Zone. The skeleton curves of the rod specimens with different lengths of the tension zone under the repeated loading mode NM19 were analyzed. As depicted in Figure 19, the length of the tension zone has a significant influence on the skeleton curve of the Q460 specimens. It can be concluded from Figure 19(b) that in the reverse compression loading stage, as the length of the tension zone of the specimen increases, the deterioration of the skeleton curve becomes more significant and the strength degradation becomes more evident. Moreover, from Figure 19(c), in comparison with the forward tensile loading, specimens RM-5, RM-6, and RM-7, which have large tensile lengths are less rigid in the reverse compression loading stage and their skeleton curves deteriorate substantially. These results indicate that the peak load and curve envelope area of the specimens decrease with the length of the tension zone when the length of the tension zone is greater than 50 mm. However, when the length is less than 50 mm, it has less influence on the skeleton curve of the specimen.

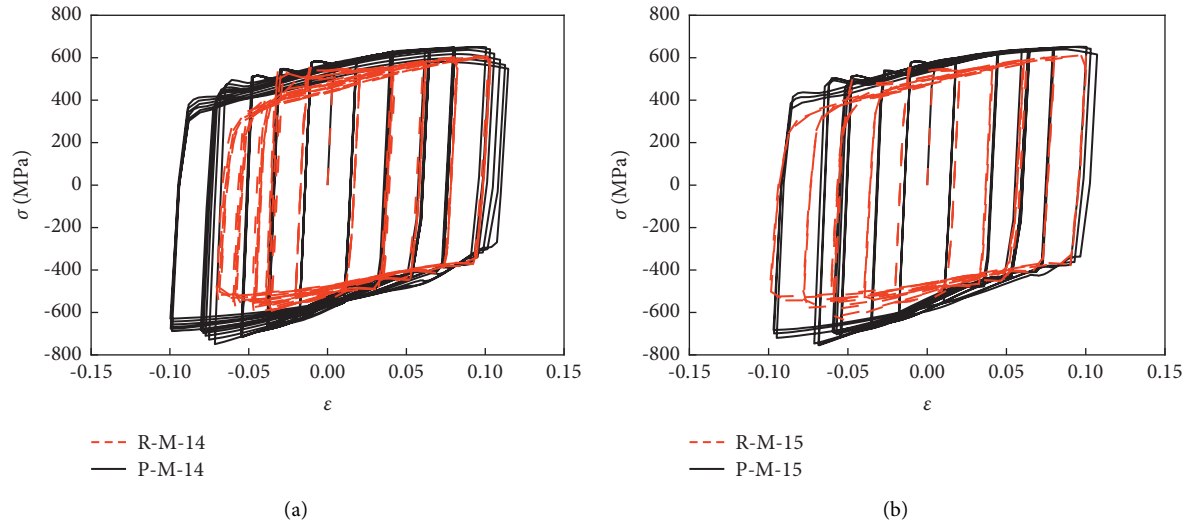

Figure 18: Hysteresis curves of material specimens with different cross section shapes. (a) Hysteresis curves of specimens under the loading pattern NM20. (c) Hysteresis curves of specimens under the loading pattern NM21.

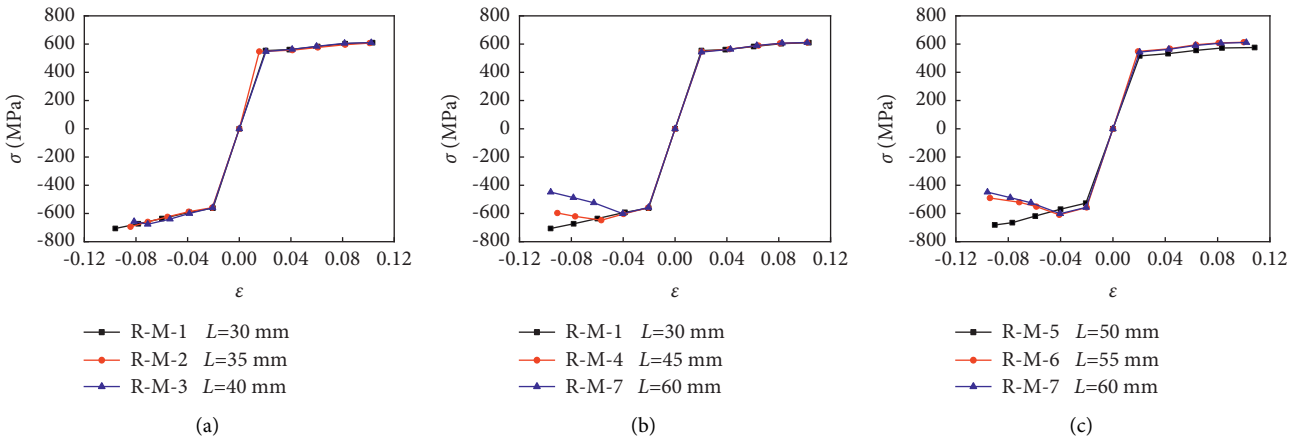

Figure 19: Skeleton curves of material specimens with different lengths in the tensile zone. (a) Specimens with a small length in the tension zone. (b) Specimens with larger length in the tension zone. (c) Specimens with large length in the tension zone.

4.4.2. Influence of the Diameter of the Tension Zone. The skeleton curve of the group R rod specimens with different diameters in the tensile zone under the repeated loading mode NM19 was analyzed (Figure 20). From the analysis of Figure 20(a), in the reverse compression loading stage, the peak load and envelope area of the curve decrease as the diameter of the tension zone is reduced for specimens RM-8, RM-9, and RM-5, which have smaller tension zone diameters. The skeleton curve deteriorates considerably. Figure 20(b) reveals that the diameter of the tension zone has a major influence on the skeleton curve of the Q460 specimens. In the reverse compression loading stage, the smaller the diameter of the specimen, the more pronounced the deterioration of the skeleton curve and the more obvious the decrease in its strength. As can be observed in Figure 20(c), specimens R-M-5, R-M-10, and R-M-11, which have large diameters in the tension zone and small diameter differences, do not exhibit a significant difference in their skeleton curves. This indicates that the diameter of the tension zone has a major influence on the skeleton curve of the specimen when the diameter of the tensile zone of the specimen is less than 10 mm. As the diameter of the tension zone decreases, the bearing capacity and energy consumption of the specimen also decrease gradually.

4.4.3. Effect of Cross-Sectional Shape. The skeleton curves of specimens with different cross-sectional shapes were plotted and evaluated (refer to Figure 21). Figure 21(a)–21(c) depict the skeleton curve comparisons for the plate specimens and the rod specimens under the equal-amplitude repeated loading mode (NM19 and NM20) and the variable amplitude repeated loading mode NM21. In comparison with the results of the rod specimen of the same area, the rigidity of the plate specimen is larger, curve degradation of the later stage of loading is flatter, and strength and energy consumption are greater. These indicate that the skeleton curve of the specimen is affected by the cross-sectional shape.

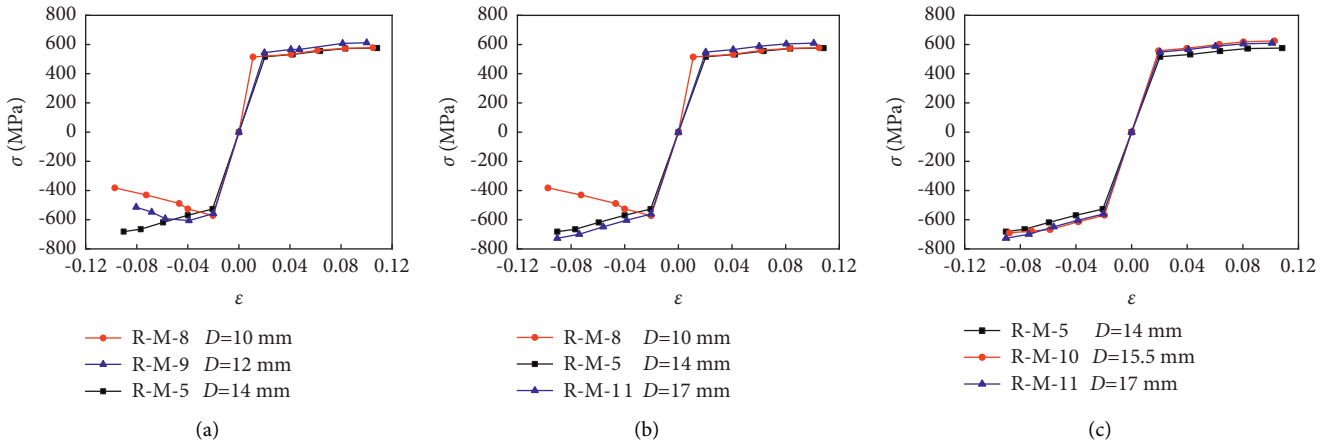

Figure 20: Skeleton curves of material specimens with different diameters in the tensile zone. (a) Specimens with a small diameter in the tension zone. (b) Specimens with large diameter in the tension zone. (c) Specimens with larger diameter in the tension zone.

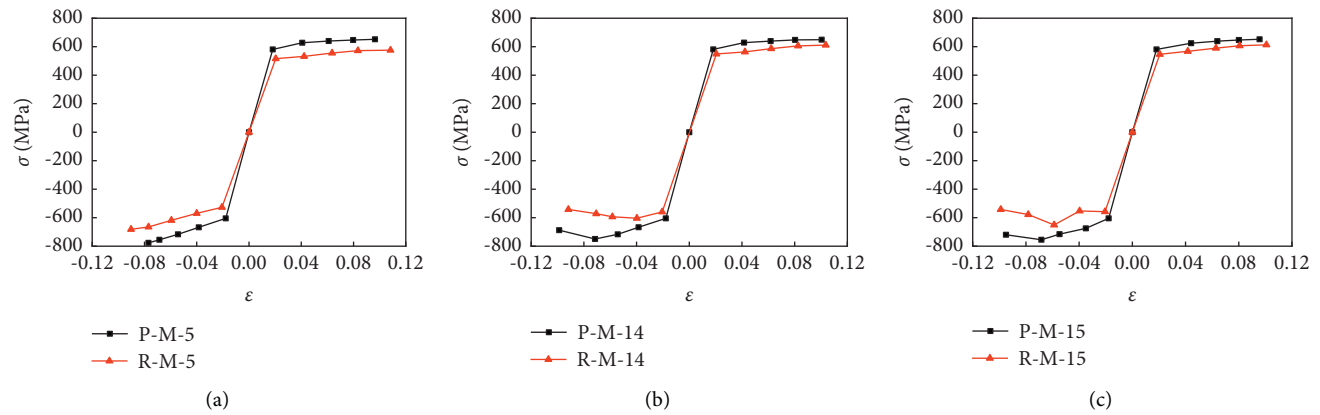

Figure 21: Skeleton curves of material specimens with different cross section shapes. (a) Specimens under the loading pattern NM19. (b) Specimens under the loading pattern NM20. (c) Specimens under the loading pattern NM21.

4.4.4. Impact of the Loading Mechanism. The skeleton curves of the plate specimens of groups P and R in different loading modes were evaluated. As depicted in Figure 22, as the number of loading cycle increases, the decrease in strength of the specimen in the later loading stages becomes more evident. Therefore, with the increase in the number of loading cycles, the effect of fatigue accumulates continuously in the specimens, thereby causing a significant decrease in strength.

4.5. Analysis of Stiffness Degradation. To study the degradation in stiffness of Q460 under repeated loading, the secant stiffness was used to quantitatively analyze the stiffness degradation of the specimens. The calculation formula of the secant stiffness K is

$$K = \frac{|+\sigma| + |-\sigma|}{|+\varepsilon| + |-\varepsilon|}, \quad (1)$$

where $+\varepsilon$ and $-\varepsilon$ are tensile strain and compressive strain at each displacement loading, respectively, where as $+\sigma$ and $-\sigma$ are the stress values corresponding to $+\varepsilon$ and $-\varepsilon$.

4.5.1. Influence of the Length of the Tension Zone. The secant stiffness diagrams for the rod specimens of groups P and R under the repeated loading mode NM19 were analyzed. As depicted in Figure 23(a), the initial stiffness of specimen P-M-7 is larger than those of specimens P-M-1 and P-M-4, and the rate of stiffness degradation is faster. This indicates that the length of the tension zone has a considerable influence on the secant stiffness of the plate specimen. The larger the length of the tension zone, the greater the initial stiffness and performance degradation of the specimen. It can be observed from Figure 23(b) that the secant stiffness behaviors of specimens P-M-1 to P-M-3 are almost coincident. This implies that the length of the tension zone has less influence on the initial secant stiffness and degradation rate when the length of the tension zone of the specimen is less than 40 mm. Moreover, from Figure 23(c), a large difference in stiffness degradation rate at the end of loading between the group R specimens was observed. Hence, the length of the tension zone has a greater influence on the stiffness degradation of the rod specimens during the later stages of loading. The greater the length of the tension zone, the more pronounced the degree of stiffness degradation.

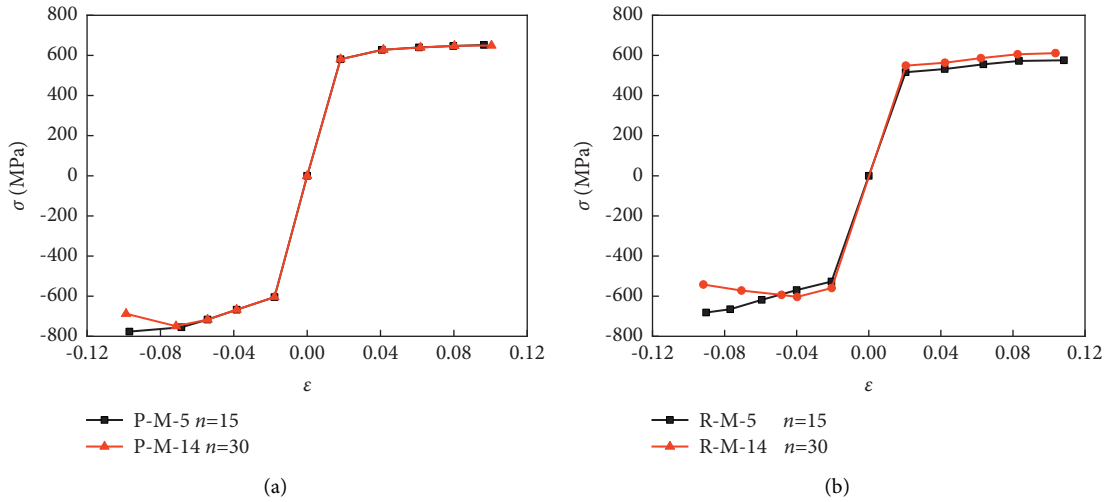

FIGURE 22: Skeleton curves of material specimens under different loading patterns. (a) Specimens P-M-5 and P-M-14. (b) Specimens R-M-5 and R-M-14.

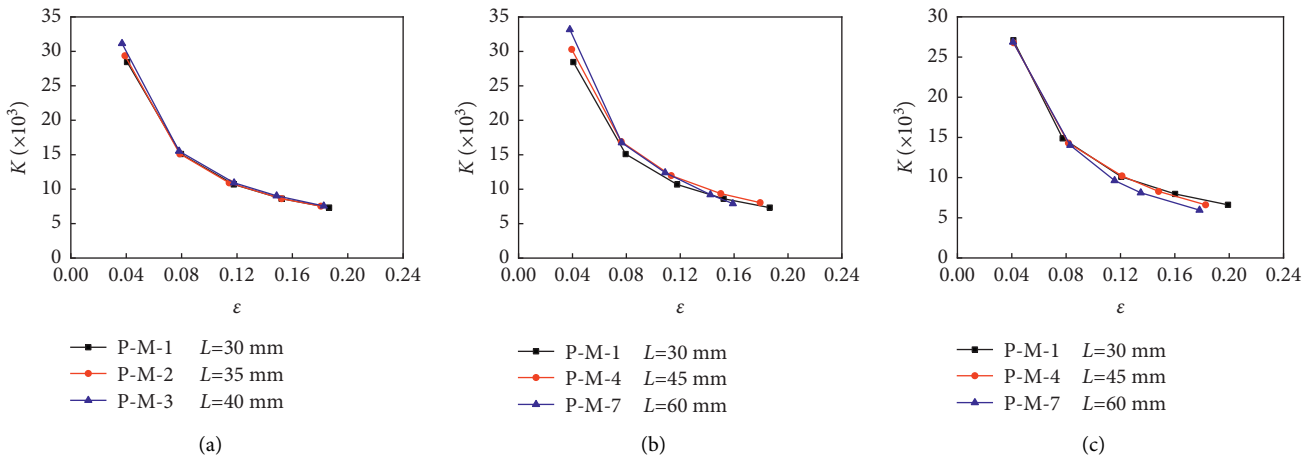

FIGURE 23: Stiffness degradation of material specimens with different tensile lengths. (a) Specimens with small length in the tension zone. (b) Sheet-shaped specimens with larger length in tension zone. (c) Rod-shaped specimens with larger length in tension zone.

Thus, the stiffness degradation of the specimen is affected by the length of the tension zone.

4.5.2. Influence of the Size of the Tension Zone. The secant stiffness diagrams for specimens with different dimensions of tension zones loaded with the repeated loading mode NM19 are illustrated in Figure 24. It can be observed from Figure 24(a) that the initial stiffness of specimen P-M-8 is larger than those of specimens P-M-9 and P-M-10, and at the later loading stages, the curves of these three specimens are nearly consistent. These observations indicate that the smaller the thickness of the plate specimen, the greater the initial stiffness. Meanwhile, the thickness has less influence on the stiffness of the plate specimen during the later stages of repeated loading. It is evident from Figure 24(b) that the initial stiffness of specimen R-M-8 is considerably higher than those of specimens R-M-10 and R-M-11. In addition, the stiffness of specimen R-M-8 degrades more rapidly at the later loading stage. This indicates that the smaller the diameter of the rod specimen, the greater the initial stiffness. Moreover, the degradation rate of the specimen during the later loading stages is faster than that of the plate specimen. Therefore, the thickness of the plate specimen and the diameter of the rod specimen have varying degrees of influence on the specimen stiffness.

4.5.3. Effect of Cross-Sectional Shape. The secant stiffness diagrams for plate specimens and rod specimens with the same loading mode are plotted in Figure 25. As shown, the initial stiffness of the group P specimens is larger than that of the group R specimens and the secant stiffness degradation of the group P specimens is more gradual. Hence, the initial stiffness of the plate specimens is greater than that of the rod specimens. In addition, during the later stages of repeated loading, the stiffness of the plate specimen deteriorates more gradually.

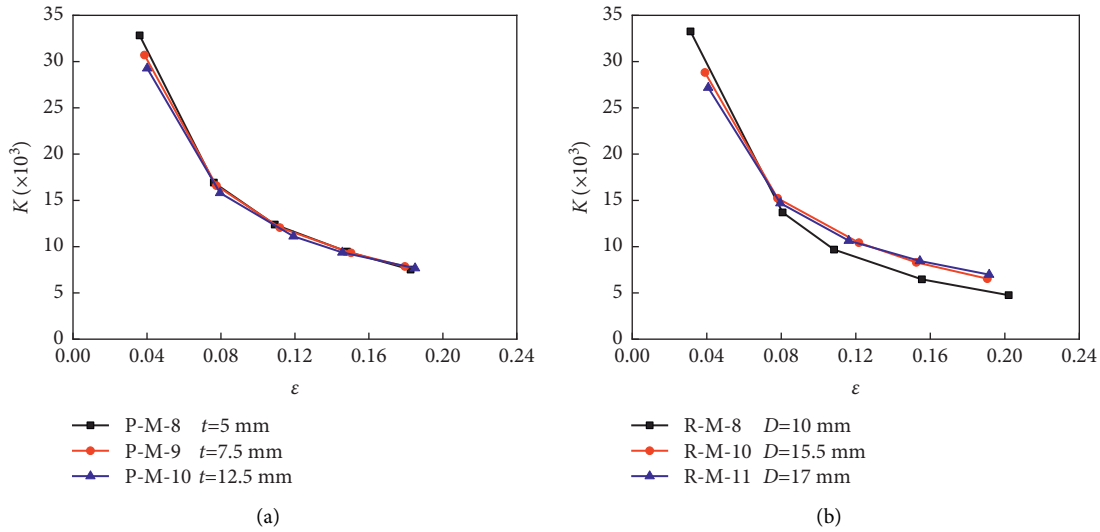

Figure 24: Secant stiffness of material specimens with different cross sections. (a) Specimens in group P. (b) Specimens in group R.

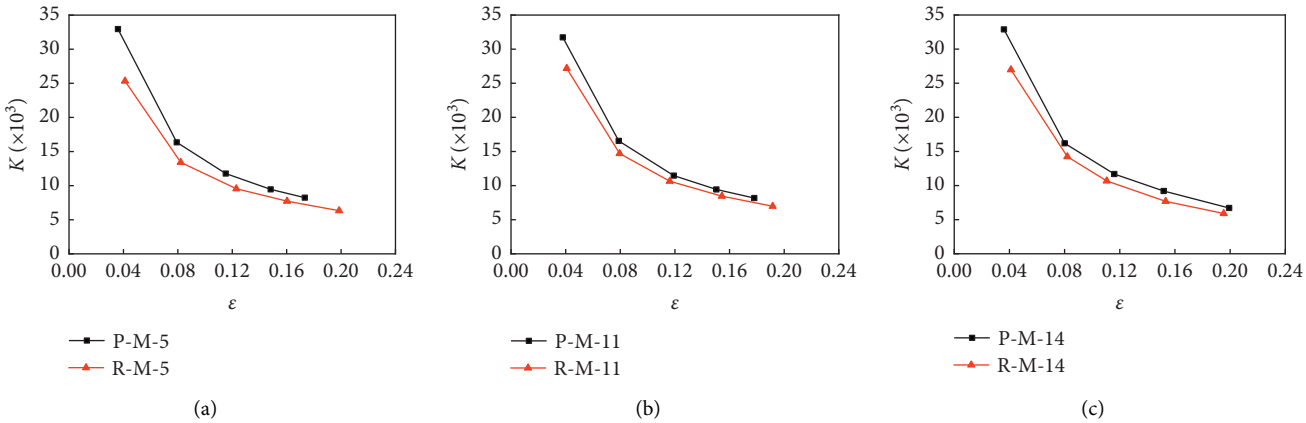

Figure 25: Secant stiffness of material specimens with different cross section shapes. (a) Standard material specimens. (b) Specimens under the loading pattern NM19. (c) Specimens under the loading pattern NM20.

5. A Model for Tensile Strength

Finite element simulation analyses for high-strength steel under repeated loading conditions are complicated. Moreover, it is difficult to directly calculate the tensile strength of high-strength steel specimens under repeated loading. To facilitate the application of Q460 high-strength steel materials in earthquake engineering based on the experimental research and numerical analysis results, a formula for calculating the tensile strength f_u of Q460 steel under repeated loading is derived. It is noted that the effect of welding is not considered in the equation

$$\varphi\left(\frac{\varepsilon_y'}{\varepsilon_{\max}}\right) + \lambda\left(\frac{f_y'}{f_u'}\right) = 1, \tag{2}$$

where ε_y' is the yield strain measured during uniaxial tension of a Q460 high-strength steel specimen, f_y' is the yield strength measured by uniaxial tension, $\varepsilon_{\max}$ is the maximum strain value applied in loading patterns (NM1, NM2, etc), and fu' is the tensile capacity of the material under repeated loading. Based on the experimental and finite element simulation results, we used the Levenberg–Marquardt method and universal global optimization method to fit the formula and finally obtained the optimal values of the parameters φ and λ. φ and λ are parameters related to the length (L) and thickness (t) or diameter (D) of the tensile zone of the specimen. n is the number of loading cycles. $\varphi = -7.1025 + 0.1415L - 0.0138t + 0.0009n$ and $\lambda = 2.6714 - 0.0317L + 0.0081t - 0.002n$. It is noted that the value of t is parallel thickness for sheet-shaped specimens, while the value of t is parallel diameter for rod-shaped specimens.

The values of the tensile strength fu' of the Q460 steel specimens under repeated loading were calculated using formula (2). And a comparison of f_u'/f_y' was made between the test results and finite element analysis results. As depicted in Figure 26, the errors between the data from formula (2) and the experimental test results are less than 4%. Furthermore, the errors in comparison with the finite element model results are less than 6%, indicating that the

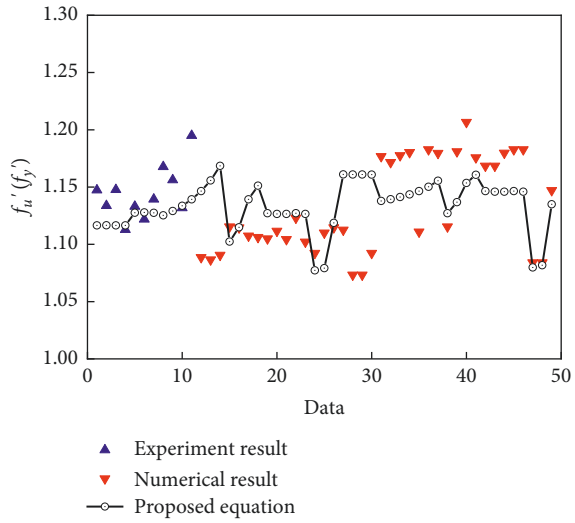

Figure 26: Comparison results by equation (2) and test and simulation.

formula (2) can accurately calculate the tensile strength of Q460 steel under repeated loading.

6. Conclusion

To investigate the mechanical properties of Q460 steel and its weld zone, an experimental study was conducted on Q460 specimens with welded joints under repeated tension and monotonic tension. The stress-strain curve and skeleton curve of the specimen with different specimen thicknesses, welding connections, and loading modes were obtained through experimental tests, and the mechanical properties of the Q460 steel specimen were analyzed. From the experimental results, it was found that the mechanical properties of welded specimens with welded joints are affected by the thickness of the specimen and the strength of the steel. In particular, for Q460 specimens welded with different consumables, the specimen welded with higher strength materials presents better ductility but has lower tensile strength.

Moreover, a finite element simulation model of Q460 specimen under repetitive loading mode was established, and skeleton curves of the specimen were obtained. The analysis found that reducing the length of the tension zone of the Q460 specimens and increasing the cross-sectional area can improve its energy-consumption and plastic deformation capabilities. In addition, for the same cross-sectional area and loading mode, the energy consumption of the plate specimens is superior to that of the rod specimens. Furthermore, the stiffness degradation of the specimen was quantitatively analyzed by secant stiffness, and the length, size, and cross-sectional shape of the tensile zone all affected the stiffness of the specimen.

Finally, based on the experimental research and numerical analysis results, the design formula for the calculation of tensile strength of Q460 under low-cycle fatigue load is proposed, which can provide a reference for its application in seismic engineering.

Nomenclature

t: Thickness of specimen
σ: Cross-sectional stress of the specimen
E: Elastic modulus of the specimen
f_y: Yield stress
f_u: Maximum tensile stress
ε_u: Strain corresponding to the maximum tensile stress fu
ε_y: Yield strain
ε: Corresponding strain when the tensile strength drops by 15%
f_y/f_u: Yield ratio
W: Elongation
E_m: Hysteresis energy
N: Number of cycles
L: Parallel length of the sheet-like specimen
D: Diameter of rod-shaped specimen
$+\varepsilon$: Tensile strain at each displacement loading
$-\varepsilon$: Compressive strain at each displacement loading
$+\sigma$: Stress values corresponding to $+\varepsilon$
$-\sigma$: Stress values corresponding to $-\varepsilon$
ε_y': Yield strain measured during uniaxial tension of a Q460 high-strength steel specimen
f_y': Yield strength measured by uniaxial tension
ε_{max}: Maximum strain value applied in loading patterns
f_u': Tensile capacity of the material under repeated loading.

Data Availability

The data used to support the findings of this study are available from the corresponding author upon request.

Conflicts of Interest

The authors declare that they have no conflict of interest.

Acknowledgments

This study was supported by Middle-aged Teachers in Education and Science Research of Fujian Province (No. JAT200825), Science Research Project in Xiamen Institute of Technology (Nos. KYT2020001 and KYZX2021010), and National Science Foundation of China (No. 51778248).

References

[1] J. W. Dai, Z. Qu, C. X. Zhang, and X. R. Weng, "Preliminary investigation of seismic damage to two steel space structures during the 2013," *Lushan earthquake Earthquake Engineering and Engineering Vibration*, vol. 12, no. 3, pp. 497–500, 2013.

[2] R. Bjorhovde, "Development and use of high performance steel," *Journal of Constructional Steel Research*, vol. 60, no. 3-5, pp. 393–400, 2004.

[3] X. C. Lin, M. Kato, L. X. Zhang, and M. Nakashima, "Quantitative investigation on collapse margin of steel high-rise buildings subjected to extremely severe earthquakes," *Earthquake Engineering and Engineering Vibration*, vol. 17, no. 3, pp. 445–457, 2018.

[4] L. T. Hai, F. F. Sun, C. Zhao, G. Q. Li, and Y. B. Wang, "Experimental cyclic behavior and constitutive modeling of

high strength structural steels," *Construction and Building Materials*, vol. 189, pp. 1264–1285, 2018.

[5] X. Q. Yang, H. Yang, and S. M. Zhang, "Rate-dependent constitutive models of S690 high-strength structural steel," *Construction and Building Materials*, vol. 198, no. 20, pp. 597–607, 2019.

[6] G. Shi, X. Zhu, and H. Y. Ban, "Material properties and partial factors for resistance of high-strength steels in China," *Journal of Constructional Steel Research*, vol. 121, pp. 65–79, 2016.

[7] Z. Nie, Y. Q. Li, and Y. H. Wang, "Mechanical properties of steels for cold-formed steel structures at elevated temperatures," *Advances in Civil Engineering*, vol. 2020, Article ID 9627357, 18 pages, 2020.

[8] X. B. Hu, R. Chen, Y. X. Xiang, Y. F. Chen, and Q. S. Li, "Mechanical behavior of damaged H-section steel structure," *Advances in Civil Engineering*, vol. 2021, Article ID 8247670, 15 pages, 2021.

[9] M. Wang, F. X. Qiao, W. G. Yang, and L. Yang, "Comparison study on constitutive relationship of low yield point stills Q345B steel and Q460D steel," *Engineering Mechanics*, vol. 34, pp. 60–68, 2017.

[10] W. C. Li, F. F. Liao, T. H. Zhou, and H. Askes, "Ductile fracture of Q460 steel: effects of stress triaxiality and Lode angle," *Journal of Constructional Steel Research*, vol. 123, pp. pp1–17, 2016.

[11] P. Haslberger, S. Holly, W. Ernst, and R. Schnitzer, "Microstructure and mechanical properties of high-strength steel welding consumables with a minimum yield strength of 1100MPa," *Journal of Materials Science*, vol. 53, no. 9, pp. 6968–6979, 2018.

[12] I. Ozturk Yilmaz, A. Y. Bilici, and H. Aydin, "Microstructure and mechanical properties of dissimilar resistance spot welded DP1000–QP1180 steel sheets," *Journal of Central South University*, vol. 26, no. 1, pp. 25–42, 2019.

[13] J. W. Sowards, E. A. Pfeif, M. J. Connolly et al., "Low-cycle fatigue behavior of fiber-laser welded, corrosion-resistant, high-strength low alloy sheet steel," *Materials & Design*, vol. 121, pp. 393–405, 2017.

[14] Z. Peilei, G. Siyuan, L. Zhengjun, and Y. Zhishui, "Study on the hybrid laser-arc welding of 3 mm thick high-strength steel with high speed," *Materials Research Express*, vol. 6, no. 2, Article ID 026546, 2018.

[15] T. Gb, *High Strength Low alloy Structural Steels*, Standards Press of China, Beijing, China, 2018.

[16] T. Gb, *Metallic Materials-Tensile Testing-Part 1: Method of Test at Room Temperature*, Standards Press of China, Beijing, China, 2010.

[17] Gb, *Code for Welding of Steel Structures*, China Construction Industry Press, Shanghai, China, 2011.

[18] W. W. Luo, H. F. Li, and B. A. Cao, "Mechanical properties of open-cell Q460 high-strength steel under tensile tension in large strain cycles," *Journal of Building Materials*, vol. 24, no. 06, pp. 1291–1299, 2021.

[19] H. F. Li, K. D. Lv, and R. S. Cui, "Seismic behavior of eccentrically compressed steel-box bridge-pier columns with embedded energy-dissipating shell plates," *Bulletin of Earthquake Engineering*, vol. 18, pp. 3401–3432, 2020.

[20] Y. Guo, C. Fang, and Y. Zheng, "Post-fire hysteretic and low-cycle fatigue behaviors of Q345 carbon steel," *Journal of Constructional Steel Research*, vol. 187, Article ID 106991, 2021.